

Research Article: New Research | Integrative Systems

Phase Gradients and Anisotropy of the Suprachiasmatic Network: Discovery of Phaseomes

https://doi.org/10.1523/ENEURO.0078-21.2021

Cite as: eNeuro 2021; 10.1523/ENEURO.0078-21.2021

Received: 5 February 2021 Revised: 2 August 2021 Accepted: 3 August 2021

This Early Release article has been peer-reviewed and accepted, but has not been through the composition and copyediting processes. The final version may differ slightly in style or formatting and will contain links to any extended data.

Alerts: Sign up at www.eneuro.org/alerts to receive customized email alerts when the fully formatted version of this article is published.

Copyright © 2021 Yoshikawa et al.

This is an open-access article distributed under the terms of the Creative Commons Attribution 4.0 International license, which permits unrestricted use, distribution and reproduction in any medium provided that the original work is properly attributed.

- 1 Title: Phase Gradients and Anisotropy of the Suprachiasmatic Network:
- 2 Discovery of Phaseomes
- 3
- 4 Abbreviated Title: Suprachiasmatic Nucleus Phaseomes and Anisotropy
- 5

6 Authors

- 7 Tomoko Yoshikawa, Scott Pauls, Nicholas Foley, Alana Taub, Joseph LeSauter,
- 8 Duncan Foley, Ken-Ichi Honma, Sato Honma, *Rae Silver

10 Affiliations

- 11 Tomoko Yoshikawa, Organization for International Education and Exchange
- 12 University of Toyama, Toyama 930-8555, Japan

13

9

Scott Pauls, Department of Mathematics, 6188 Kemeny Hall, Dartmouth College,Hanover, NH, 03755 USA

16

23

- 17 Nicholas Foley, Department of Mathematics, 6188 Kemeny Hall, Dartmouth College,
- 18 Hanover, NH, 03755. Department of Neuroscience and Zuckerman Mind Brain Behavior
- 19 Institute, Columbia University, 3227 Broadway, New York City, NY, 10027, USA 20
- Alana Taub, Department of Neuroscience, Barnard College, New York City, NY, 10027,
 USA
- Joseph LeSauter, Department of Neuroscience, Barnard College, New York City, NY,
 10027, USA
- Duncan Foley, Department of Economics, New School for Social Research, New York
 City, NY, 10011, USA
- 30 Ken-Ichi Honma, Research and Education Center for Brain Science, Hokkaido
- 31 University, Sapporo, 060-8638, Japan. Center for Sleep and Circadian Rhythm
- 32 Disorders, Sapporo Hanazono Hospital, Sapporo, 064-0915, Japan.

- Sato Honma, Research and Education Center for Brain Science, Hokkaido University,
 Sapporo, 060-8638, Japan. Center for Sleep and Circadian Rhythm Disorders, Sapporo
 Hanazono Hospital, Sapporo, 064-0915, Japan.
- 37
- *Rae Silver, Department of Neuroscience, Barnard College, 3009 Broadway, New York
 City, NY, 10027, USA.; Department of Psychology, Mail Code 5501, Columbia
- 40 University, 1190 Amsterdam Avenue, New York City, NY, 10027, USA., Department of
- 41 Pathology and Cell Biology, Graduate teaching faculty, Columbia University Medical
- 42 School, New York City, NY, 10032 USA.

4344 *Corresponding author: Rae.Silver@Columbia.edu

- 45 Number of figures: 4
- 46 Number of tables: 0
- 47 Number of words
- 48 Abstract: 201
- 49 Significance Statement: 120
- 50 Introduction: 812
- 51 Discussion: 1211
- 52 Extended Data
- 53 Number of figures: 454
- 55 **Keywords**: circadian, phase waves, network, vasopressin, vasoactive intestinal
- 56 peptide, oscillation

57 58

- 59 Acknowledgments: The research was funded in part by grants from NSF | BIO |
- 60 Division of Integrative Organismal Systems (IOS) 1256105; 1749500 (to RS and SP)
- and by JSPS KAKENHI (Grant 19K06774 to TY). TY thanks Dr. H. Gainer (National
- 62 Institutes of Health) for the generous donation of AVP antibody for
- 63 immunohistochemistry and Dr. Y. Shigeyoshi (Kindai University) for helpful discussions.
- 64 Conflicts of Interest: The authors declare no competing financial interests.
- Funding sources: This work was supported by National Science Foundation Grants
 1256105 and 1749500 (to R.S.).

67 Author Contributions

- 68 TY SPJLS AT conducted the experiments;
- 69 TY RS SP DF JLS designed the experiments
- 70 RS SP NF DF analyzed the data
- 71 RS SP NF SH KH JLS DF wrote the paper.

72 73

74

75

76 Visual Abstract

- 77 78
- 79 Insert Visual Abstract here

80

- 0.1
- 81 82

83 Abstract

84 Biological neural networks operate at several levels of granularity, from the individual 85 neuron to local neural circuits to networks of thousands of cells. The daily oscillation of the brain's master clock in the suprachiasmatic nucleus (SCN) rests on a yet to be 86 87 identified network of connectivity among its ~20,000 neurons. The SCN provides an 88 accessible model to explore neural organization at several levels of organization. To 89 relate cellular to local and global network behaviors, we explore network topology by 90 examining SCN slices in three orientations using immunochemistry, light and confocal 91 microscopy, real-time imaging, and mathematical modeling. Importantly, the results 92 reveal small local groupings of neurons that form intermediate structures, here termed 93 "phaseoids" which can be identified through stable local phase differences of varying 94 magnitude among neighboring cells. These local differences in phase are distinct from 95 the global phase relationship – that between individual cells and the mean oscillation of 96 the overall SCN. The magnitude of the phaseoids' local phase differences are 97 associated with a global phase gradient observed in the SCN's rostral-caudal extent. 98 Modeling results show that a gradient in connectivity strength can explain the observed 99 gradient of phaseoid strength, an extremely parsimonious explanation for the 100 heterogeneous oscillatory structure of the SCN. 101

102 Significance statement

103 Oscillation is a fundamental property of information sensing and encoding in the brain. 104 Using real time imaging and modeling, we explore encoding of time by examining 105 circadian oscillation in single neurons, small groups of neurons, and the entire nucleus, 106 in the brain's master: the suprachiasmatic nucleus. New insights into the network 107 organization underlying circadian rhythmicity include the discovery of intermediate 108 structures, termed 'phaseoids', characterized by groups of neurons which are stably out 109 of phase with their neighbors. Modeling indicates that the pattern of phaseoids across 110 the tissue encompasses a gradient in connectivity strength from the rostral to caudal 111 aspects of the nucleus. Anisotropy in network organization emerges from comparisons 112 of phaseoids and connectivity gradients in sagittal, horizontal and coronal slices. 113

115 Introduction

116 It is widely accepted that the phasing of neuronal oscillation is an important aspect of 117 network organization and brain function (Buzsaki & Draguhn, 2004). The hypothalamic 118 suprachiasmatic nuclei (SCN) function as a master circadian clock that orchestrates 119 circadian rhythms in behavior and physiology. Each SCN is made up of ~10,000 120 neurons and the individual neurons contribute to circuits that support the coherent daily 121 oscillation of the nucleus. While most SCN neurons express circadian oscillations, the 122 individual cellular rhythms in the network are not synchronized in that they do not 123 simultaneously reach peak phase (Schaap et al., 2003; Evans et al., 2011; Koinuma et 124 al., 2013). Orchestration of stable circadian rhythmicity requires a network that couples 125 individual SCN neurons to each other (Indic et al., 2007; Webb et al., 2009; Honma et 126 al., 2012; Abel et al., 2016; Hastings et al., 2018; Tokuda et al., 2018; Wang et al., 127 2018; Finger & Kramer, 2020)

128 With respect to circadian timing, a challenge is to understand how coherent daily 129 rhythms emerge in the brain master clock through interactions of its individual neurons, 130 ensembles of neurons, and larger-scale oscillation of the SCN tissue as a whole. 131 Substantial evidence indicates that stable phase differences occur not only between 132 adjacent neurons (Quintero et al., 2003) but also among clusters of neurons in 133 subregions of the nucleus (Yan & Okamura, 2002; Yamaguchi et al., 2003; Inagaki et 134 al., 2007; Brown & Piggins, 2009; Evans et al., 2011; Foley et al., 2011; Pauls et al., 135 2014; Yoshikawa et al., 2017). While peak phase differs among neurons, relative phase 136 does not drift (Yamaguchi et al., 2003), pointing to a non-uniform SCN network topology 137 underlying tissue-wide oscillation.

138 Instead of synchronization of peak phase among individual elements, long-term, real-139 time luciferase reporter imaging of clock genes or proteins in SCN slices indicate phase 140 waves that propagate over the entire nucleus with a ~24-hour rhythm. In coronal 141 slices, these daily phase waves generally start in a distinct cluster of neurons in the 142 arginine vasopressin- (AVP-) rich dorsal or dorsomedial region of the nucleus (Evans et 143 al., 2011; Enoki et al., 2012). It is noteworthy that there are marked differences in 144 oscillatory patterns among slices, likely due to inclusion of different network components 145 included at the time of tissue harvesting. Within an individual slice however, the phase 146 relationships of serial oscillatory waves are stable if the tissue is not perturbed (Foley et 147 al., 2011). An important question is how these phase patterns link to the underlying 148 fixed aspects of the SCN network. The localization of major clusters of SCN peptides do 149 not fully explain the patterns of oscillation (Evans et al., 2011), and the precise topology of the SCN connectome has been difficult to establish in part because of the small size, 150 151 dense packing and heterogeneity of its neurons and the fine caliber of fibers (Van den 152 Pol, 1980).

153 While understanding of the intra-SCN connectome is incomplete, the functional

154 significance of the connections between two major regions, namely the ventral core and

dorsal shell are well established (reviewed in (Honma, 2018)). The core-shell framework

has produced both biological and modeling work that provides substantial insight into

157 SCN oscillation (reviewed in (Pauls *et al.*, 2016)). An aspect of network topology that

escapes notice in studies of core-shell relationships is the possibility that SCN networks
 are anisotropic and that key aspects of network topology are lost following transection of
 fibers that course rostro-caudally. Studies of other oscillatory networks, such as the
 thalamus, highlight the principle that network oscillatory properties differ when brain

sections are cut in the transverse versus the longitudinal axes (Gloveli et al., 2005).

163 The goal of this study was to determine whether fixed properties of SCN tissue. 164 specifically those set by the localization and connectivity of its neurons might underlie 165 the observed SCN oscillatory phase patterns and their variations. How the intact 166 SCN's anatomy, morphology, connectivity gives rise to the phase relationships among 167 SCN neurons or clusters of neurons remains elusive. Also elusive is how circadian 168 oscillation is retained following ablation of major components of the nucleus (Rusak, 169 1977; LeSauter & Silver, 1999). To address some of the caveats in our understanding, 170 we pair detailed morphological analyses of fixed tissue, studies of real time imaging of 171 PER2::LUC expression in cultured SCN tissue and mathematical and statistical tools 172 to explore SCN networks. We define the biological aspects of SCN organization that 173 underlie the topography of individual cellular oscillations and investigate the impact of 174 that evidence on simulations with a mathematical model. The biological results point to 175 novel intermediate structures that we term 'phaseoids'. Sagittal and horizontal slice 176 orientations that maintain the SCN's rostral-caudal axis reveal a global phase gradient 177 associated with the magnitude of the local phase differences within the phaseoids. 178 Modeling results show that a gradient of connectivity strengths between neurons can 179 account for the observed phase gradient of the phaseoids along the rostral-caudal axis.

180 Materials and Methods

181

191

182 Visualization of SCN peptides in sagittal, coronal and horizontal planes. To visualize the distribution of peptidergic cell types in the SCN, sections were stained for 183 184 mENK, GRP, Calretinin, GFAP, dapi and AVP and VIP (the latter in colchicine treated 185 mice) using the material and protocols previously reported in (Varadarajan et al., 2018). 186 To create the schematic, the localization of peptides and dapi was based on representative sections at the largest extent of the nucleus in each plane. For sagittal 187 and coronal sections the localization of peptides and dapi was plotted based on a 188 189 representative section at the largest extent of the nucleus, for the horizontal view, the 190 data is based on previously unpublished material.

Oscillation Criteria. As PER2::LUC expression in sagittal sections has previously
 never been described, we asked whether circadian oscillation is seen in all slices
 harvested or alternatively, whether it is restricted to the slices that bore core and shell
 components. To this end, each slice was assessed to classify oscillation, independently
 by two observers. In addition, slices were evaluated using Fourier analysis to determine
 statistical significance of the 24 hr. period.

SCN slice culture, bioluminescence. <u>Slice culture</u>: Mice were decapitated and
 enucleated after cervical dislocation between zeitgeber time (ZT) 5 and 9. The brain
 was removed and chilled in ice cold Hanks' balanced salt solution, followed by slicing of
 tissue (microslicer; Dosaka EM, Kyoto, Japan) at 100µm in a sagittal, coronal or

203 horizontal plane. The brain slices were cultured on a membrane (Millicell-CM 204 membrane, Millipore) with 1.3 ml of DMEM containing 0.2 mM D-luciferin K and 5 % 205 culture supplements as in (Yoshikawa et al., 2013). Bioluminescence recording: 206 Images were obtained using a CCD camera cooled to -80 °C (ImagEM, Hamamatsu 207 Photonics, Hamamatsu, Japan; iXon3, Andor, Belfast, UK). Bioluminescence was 208 recorded hourly for six consecutive days, starting immediately after decapitation. At the 209 end of the recording period, the brain slices were fixed with 4% paraformaldehyde in 0.1 210 M phosphate buffer (PFA) and prepared for immunohistochemistry. All procedures were 211 approved by the University Animal Care and Use Committee.

212 Visualization and analysis of luciferase in serial frames of the image stacks. The 213 raw data consists of sequential images recording PER2::LUC expression over one hour 214 intervals. Data processing includes restricting the images to a region of interest thereby 215 delineating the SCN and windowing the time series to a range in which movement of the 216 tissue is minimal. Further, image sequences were restricted from the first frame without 217 movement to the longest possible multiple of 24 hours to alleviate artifacts in Fourier 218 analyses. Raw images were imported into Image J (version 1.52). For visualization 219 purposes, outliers were removed using manual observation of the histogram. The image 220 was then imported into Photoshop, converted into RGB scale and a color gradient was 221 applied. Next, the first peak of PER2::LUC expression time and each subsequent 3 hr. 222 interval was captured for a total of a 27 hr. cycle. The brightness time series was 223 computed as follows: 1) the data was restricted to the spatial ROI delineating the SCN, 224 and the temporal ROI with minimal tissue movement. 2) The whole of the remaining 225 data was then z-scored and plotted with the mean of each frame.

Only those with a robust 24 hr. period were considered for further analysis. A further screening was then done using mean brightness time series, to ensure that there were several complete circadian oscillations in each slice. All slices meeting these criteria were further analyzed. We focused on sections that contained the rostral and caudal poles, as these preserved the full rostro-caudal extent of the nucleus, and included the rostral and caudal poles that cannot be studied in coronal sections. Two slices were chosen in each orientation to illustrate the results.

233 Global scale phase map: Extracting the phase associated to the component of the

234 **signal with a 24-hour period.** For each pixel, we computed a discrete Fourier

transform of the time series (described above as a multiple of 24 hours). This results in

each pixel having a complex number, $\alpha + i \beta$, associated to the component of signal with a 24-hour period, which allows us to compute the phase:

 $\phi = \arctan(\beta/\alpha).$

Each phase is given in radians, which we can convert to hours: $\bar{\phi} = \frac{\phi}{2\pi} \cdot 24$. As phase is a relative statistic – it can only be measured against a baseline – we normalize the phases across the SCN so that a phase of zero corresponds with the mean signal across the SCN at the period of 24 hours. This results in the phase of every pixel being at most 12 hours phase advanced, or 12 hours phase delayed relative to the mean oscillation. The product of this process is a matrix *P* that aligns with the images in the frames of the PER2::LUC movies: P(x, y) is the phase extracted from the time series associated to the pixel in the (x, y) coordinate in a frame of the movie. Each lobe of the SCN was analyzed separately, and for visualization purposes, one of the two lobes was chosen for each of the horizontal and coronal slices.

248 Computing local scale phase difference with a center-surround filter.

249 Examination of the global phase maps raises the question of the extent of 250 heterogeneous phases in localized patches of the SCN. To focus on this local analysis, 251 we compare the average of phases over a cell-sized disk of pixels to an average of 252 those of an annular region surrounding that disk. This is done by convolving a filter 253 isolating each putative cell-like region with the matrix of surrounding phase estimates. 254 we use a binarized difference of Gaussians filter to facilitate the computation. Such a 255 filter is also called a center-surround filter, as it is positive on central disk and negative 256 on a surround annulus.

258 We define the filter by

$$F(x,y) = \frac{1}{2\pi\sigma^2} e^{-\frac{x^2 + y^2}{2\sigma^2}} - \frac{1}{2\pi K^2 \sigma^2} e^{-\frac{x^2 + y^2}{2K^2 \sigma^2}},$$

259 where (x, y) are the coordinates in the image plane, and σ and K are parameters that 260 delineate the center and the surround: the first term is a Gaussian with standard 261 deviation σ , defining the center, and the second a Gaussian with standard deviation $K\sigma$, 262 which defines the surround. For our purposes, using $\sigma = 1, K = 2$ creates a filter which 263 is positive on a central disk of radius 4 pixels (roughly 9 um) and a surrounding annulus 264 with outer radius 13 pixels (roughly 20 um) where the filter in negative. These sizes are 265 consistent with comparing neurons to the surrounding tissue in our data, as SCN 266 neuronal radii are 4-4.5 pixels. Further, we binarize and normalize this filter by first replacing all values with absolute value less than 10^{-5} with zero. Then we replace the 267 268 remaining positive values with +1 and negative values with -1. Last, we normalize the 269 negative values of the filter by dividing by the number of pixels with a negative value 270 and the positive values similarly. We denote the resulting filter by $\overline{F}(x, y)$. The circular 271 annulus around a cell-like center we chose is based not only on patterns observed in 272 the tissue but also because it is a general filtering approach used as a pre-processing 273 technique for such problems as edge detection (Canny, 1986).

274

257

275 Convolution of the center-surround kernel over the SCN. Convolving with this filter 276 provides the difference in average phases between the disk and surrounding annulus 277 centered at each pixel in the image. Applying center-surround filter to the SCN using 278 2D-convolution, $D = P \star \overline{F}$, measures phase difference in the time series between each 279 local disk and its nearest neighbors. The entry D(x, y) gives the difference between the 280 average of the phases over the central disk of the filter, translated to be itself centered 281 at the coordinates (x, y), and the average of the phases over the annular part of the 282 filter. 283

284 Prior to implementing this method, we benchmarked the algorithm by evaluating

- whether it detected the visually identified rings. In looking at the PER2 expression
- 286 movies, we noticed roughly circular arrangements of PER2::LUC neurons that we could

287 visually detect due to brightness differences with the surrounding tissue (also seen in 288 fixed tissue). These circular arrangements were most obvious to the eye in the hours 289 around the trough of the oscillation, at times of overall low PER2::LUC expression; they 290 could not be seen at high points of PER2::LUC when the entire nucleus was bright and 291 individual neurons could not be visualized by eye. We then compared the local phase 292 difference results over the same region to assess whether the two methods matched. 293 This benchmarking procedure confirmed that visually identified phaseoids, seen over 294 several oscillations in the PER2::LUC movies, were detected by the application of the 295 center-surround filter. 296

This benchmarking procedure confirmed that visually identified phaseoids, seen over several oscillations in the PER2::LUC movies, were detected by the application of the center-surround filter by merging the PER2::LUC intensity image with the local phase difference results. Photoshop was used to create the blended image shown in Extended Data Figure 3-1.

302 303

304 **Kuramoto coupling model.** We use Kuramoto model systems to investigate the 305 possible contribution of connection strength to the existence of the rostral-caudal 306 gradient in the local phase maps. Kuramoto systems with cluster synchronization, 307 where smaller clusters of oscillators synchronize to different phases, exhibit higher intra-308 cluster and lower inter-cluster connectivity (Favaretto et al., 2017) suggesting similar 309 features might hold for the clusters of tissue we observe in the local phase maps. The 310 Kuramoto model systems comprise a set of oscillators that are connected to and 311 influence one another. Each oscillator in the system represents a neuron and is 312 characterized by its intrinsic frequency, ω_i , and the strength of its connections to other oscillators, $\{a_{i1}, a_{i2}, \ldots, a_{in}\}$. We represent the model system by a set of n differential 313 314 equations:

$$\dot{\theta_i} = \omega_i + K \sum_{j=1}^n a_{ij} \sin(\theta_j - \theta_i).$$

315 Here, K is a global underlying coupling strength. Using the Runge-Kutta method, we 316 can numerically solve this set of equations for the $\{\theta_i\}$, allowing us to test different 317 hypotheses. To look at the contribution of coupling to the rostral-caudal gradient, we 318 set up a simple testing framework. First, oscillators are arranged on a grid and 319 connected to their nearest neighbors. Second, we vary the strength of the connectivity 320 in one direction to evaluate the effects of strength on the patterns of the resulting 321 phases of the oscillators. To formalize this, we construct a model using a 20×20 grid of 322 oscillators arranged on a planar lattice. We set the intrinsic frequencies to be the same, $\omega_i \equiv 2\pi/24$, and K = 5. Letting (x(i), y(i)) be the planar coordinates of oscillator *i*, we 323 define $a_{ij} = \left(\frac{x(i)}{20}\right)^2$ whenever *i* and *j* are neighboring oscillators in the plane (i.e. 324 325 $max \{ |x(i) - x(j)|, |y(i) - y(j)| \} = 1 \}$. This change in strength across the rectangle of 326 oscillators models weaker connection strength on one side of the SCN that strengthens

327 as we move across the tissue to the other side. We solve numerically over a 240 hours

period, in steps of 1 minute after providing initial conditions that are picked uniformly at random from $[-\pi, \pi)$.

330

349

331 **Results**

332 Visualization of SCN in three planes: The SCN is made up of a heterogeneous population of neurons. To set the stage for understanding the relationship of regionally 333 334 specific clusters of cell types to the SCN network topology, we first mapped the 335 peptidergic organization of the mouse SCN, delineating the major peptidergic cell types 336 that can be retained when SCN tissue is prepared in sagittal, horizontal or coronal orientations (Fig. 1A). The SCN is a bilateral structure, lying on each side of the 3rd 337 338 ventricle and extending approximately 350µm dorsoventrally, 300µm laterally from the 339 third ventricle and 700-750µm rostrocaudally (including a finger-like rostral projection). 340 The full rostro-caudal extent of the SCN is best seen in sagittal sections. The 341 distribution of these key peptides aligns fully with the spatial distribution of 342 corresponding genes (Wen et al., 2020). The peptide maps in Fig. 1 emphasize that the 343 specific SCN neurons and networks captured when tissue is sectioned for ex vivo real 344 time imaging of oscillation can differ markedly depending on the precise tilt of the brain 345 when it is blocked and on the orientation in which it is sliced. These differences among 346 slices provoke the question of which cellular and network components are necessary for 347 oscillation and whether anisotropy (directionality) is a determinant of the pattern of SCN 348 oscillation.

350 Effect of slice orientation on oscillation. We compared the effect of transecting SCN 351 networks in three orientations by examining oscillation of PER2::LUC in sagittal, coronal 352 and horizontal slices (Fig. 1B, middle panel). Imaging of sagittal sections has not 353 previously been reported. For this reason, we first examined whether the results seen in 354 these slices correspond to data on PER2 expression in immunochemically stained 355 sagittal sections harvested from animals sacrificed at specific circadian time points 356 (Extended Data Fig. 1-1). The results are confirmatory: The peak and trough oscillations 357 are separated by ~12 hrs., and the overall oscillation has a period of ~24 hrs (see 358 pseudocolored images of changes over time and quantification of the brightness time 359 series in Fig. 1B, left and right respectively). The oscillation of the caudal SCN is more 360 marked than the rostral aspect, and bears a different phase. The results for oscillation in 361 our coronal and horizontal sections are consistent with previous reports on real time 362 imaging of SCN slices (Evans et al., 2011; Yoshikawa et al., 2017). 363

364 For real time imaging of the sagittal slices, we next investigated whether the anatomy of 365 the slice, determined after imaging, impacted the production of oscillation or whether all 366 slices oscillated irrespective of which circuit elements were present in the tissue. The 367 results indicate that slices bearing both AVP and VIP neurons had robust rhythmicity 368 while those lacking these peptides were not rhythmic (Extended Data Figure 2-2, see 369 methods for oscillation criteria). Slices bearing a large number of AVP neurons but 370 lacking VIP were not rhythmic, consistent with previous reports in coronal slices (LeSauter & Silver, 1999; Aton et al., 2005). 371

373 Insert Fig. 1 around here

374 375 376

Legend Fig. 1: Architecture and PER2 expression of the SCN and Bioluminescence heat maps and brightness time series

377 A. Depiction of the peptidergic architecture by analysis of single-labelled SCN peptides in sagittal, coronal 378 and horizontal planes. The localization of the major peptides of the SCN is shown in each orientation. The 379 vertical and horizontal lines in the sagittal section indicates the plane shown in the adjacent cartoons of 380 coronal and horizontal sections. Dapi label represents cells that are not positive for any of the markers 381 used. Vasoactive intestinal polypeptide (VIP)-containing neurons lie in the ventral core area. AVP 382 neurons lie in the rostral protrusions and in much but not all of the outer borders of the nucleus. A gastrin-383 releasing peptide (GRP)-rich area, along with nearby glial fibrillary acidic protein- (GFAP-) positive 384 elements, lies between the VIP core and AVP shell. In coronal sections, the localization of core (VIP- and 385 GRP-rich) and shell (AVP-rich) regions are seen. In horizontal sections, the precise peptidergic content of 386 an SCN slice differs markedly depending on the angle and depth at which the SCN is cut; if the ventral 387 aspect is included in a slice, then both the core and shell are represented. B. The spatiotemporal pattern 388 in PER2::LUC bioluminescence in SCN slices is shown at 3-h intervals for representative sagittal, coronal 389 and horizontal slices. Time zero was defined as the time point with the lowest bioluminescent intensity 390 (see Materials and Methods for details). The pseudocolored images are normalized to the brightest image 391 of each slice. The rainbow scale (blue, low and red, high expression) for each slice lies on right side of 392 the last panel. The SCN slices are numbered consistently to correspond on all figures. All slices were 393 recorded for the same 6-day duration, starting immediately after harvesting the tissue. Mean circadian 394 oscillation used in further analysis is shown in the right column. Explanation of differences among slices 395 in the durations of data used for analysis is provided in "Methods". PER2 expression in perfused tissue 396 from animals killed at controlled times of day is shown in Extended Data Fig. 1.1.

397 398

399 Observing phaseoids using biology and mathematics: In the real time imaging 400 studies, close examination of the tissue near the trough of the oscillation reveals local 401 phase heterogeneity with small populations of cells substantially out of phase with the 402 surrounding tissue (Fig. 2A top panel). We designate these groupings as intermediate 403 structures, here termed 'phaseoids'. Phaseoids (denoted by red asterisks) are a local 404 group of cells with stable phase heterogeneity, in which a cell is surrounded by a group 405 of cells out of phase with it. A representative phaseoid from the imaged material is 406 shown at two time points with a phase difference of ~5 hours between the center cell 407 and the surrounding cells (Fig. 2A middle and bottom panels). These phaseoids are not 408 an artefact of the preparation, as they can also be seen in SCN sections from animals 409 sacrificed near the trough of PER2 protein expression.

410

411 Relation of global to local phase. To explore global and local phase gradients through 412 the full extent of the SCN, we devised a general analytical tool and applied it across 413 different slice orientations. For global phase gradients, the phase of each pixel was 414 assessed against the mean phase of the tissue (the global phase). This allowed 415 determination of the effects on oscillation of preserving limited aspects of the network. 416 Analysis of the temporal pattern of PER2::LUC expression in the slices through Fourier 417 methods allowed identification of the phase of oscillation of any region of the SCN 418 tissue relative to the mean circadian oscillation of the tissue as a whole (see Methods). 419 Using such methods, we investigated whether phase maps differ by slice orientation 420 and find that global phase maps show systematic phase anisotropy and heterogeneity 421 (Fig. 2B).

423 Phase is represented by color, ranging from small regions that are phase advanced 424 (red) or phase delayed (blue) with respect to the tissue mean (yellow). In the sagittal 425 slices, there are neurons at the rostral pole and those in an area adjacent to the core 426 that are phase delayed (blue speckled areas) relative to the mean tissue oscillation. 427 Similarly, the horizontal sections also show near anti-phase relations between the 428 rostral and caudal aspects of the tissue, with the caudal area substantially phase 429 advanced (~5 hours) and the rostral aspect of the tissue substantially phase delayed 430 (also ~5 hours) relative to the mean. In coronal sections we find, consistent with 431 previous literature, a phase advanced region in the dorsal-medial aspect of the tissue. 432 The rest of the phase map varies among slices [as previously reported (Foley et al., 433 2011; Pauls et al., 2014)], likely due to heterogeneous sampling of the circuit depending 434 on which part of the rostral-caudal extent to the slice was studied. 435

436 Insert Fig. 2 about here

437 438

454

465

Legend Fig. 2: Global phase maps and phaseoids.

439 A. Phaseoids in the SCN. The top panel is a raw image of a bioluminescent recording near the trough 440 of PER2::LUC expression in a sagittal section. Red asterisks highlight the location of phaseoids. The 441 inset shows a magnification of the phaseoid indicated by the arrow. The middle panels are 442 bioluminescent images of a phaseoid in a sagittal section taken at two time points. At time 23, 443 PER2::LUC expression is higher in the center cell compared to its neighbors. Five hours later, 444 PER2::LUC expression is higher in surrounding cells compared to the center cell. The bottom panel 445 shows the PER2::LUC oscillation over ~ 72hrs in the center cell (red circle), surround cell (green circle) 446 and the whole SCN for the phaseoid in the middle panel. B. Mathematically assessed phase maps for 447 sagittal, horizontal and coronal slices of the SCN. Phase is represented by color, ranging from regions 448 that are phase advanced (red) or phase delayed (blue) with respect to the tissue mean (yellow). The color 449 of the 12 hour advanced regions matches to those with 12 hour delayed regions, as these will be in phase 450 with one another in a 24 hr. oscillation. All sections exhibit areas that are phase advanced and others that 451 are phase delayed often intermingled with one another. The analysis of immunohistochemical staining of 452 SCN slices after imaging is shown in Extended Data Fig. 2-1. Phaseoids in fixed SCN tissue are shown in 453 Extended Data Fig. 2-2.

455 Phaseoids have not been previously reported but are consistent with prior work showing 456 that adjacent neurons can be out of phase with each other (10). Local phase behavior 457 may be a common occurrence across the SCN but could differ in structure depending on slice orientations and may be obscured by slice heterogeneity. The large global 458 459 phase differences across the tissue confounds a local analysis – phase gaps of, for 460 example, 4 hours might occur between adjacent regions with global phases at 10 hours 461 and 6 hours from the mean in one part of the slice, and between regions with phases at 462 0 and -4 hours at another area. This consideration prompted us to develop a 463 mathematical method to examine localized phase maps based on a center-surround 464 filter that exposes relative local phase differences.

466 Application of annular filter: Differences in phases can be difficult to detect by visual 467 examination of individual still images. Visual identification of phaseoids best occurs for 468 that subset in which PER2::LUC expressing cells are active during a global trough. To 469 enable phaseoid detection across the whole of the circadian oscillation, we constructed 470 a center-surround filter to report the difference between the average phase in a cell-size 471 disk of pixels around each point and that of a local annulus of equal radius around the disk (Fig. 3A, middle panel, see methods for more details of center-surround filter and
"kernel"). The local phase analysis allows the examination of phaseoids
computationally. This is illustrated by a very prominent phaseoid identified from a global
phase map in Fig. 2B that has a phase difference of about 10 hours. In a representative

example the center cell size disk (blue) phase-lags the mean oscillation by about 5
hours (Fig. 3A top panel). Surrounding it are four neuron-sized regions (red) that lead

478 the mean oscillation by about 5 hours.

479

509

480 Convolving by the filter over each pixel of the phase map results in a local analysis (Fig 481 3A bottom panel). Phaseoids vary in the differences in the phase relationships of their 482 components. The strength of the phaseoids vary across the tissue and we define the 483 'strength' of a phaseoid as the magnitude of the difference between the mean phase of 484 the center and the mean phase of the surround. For example, a weak phaseoid would 485 have a center-surround phase gap of less than an hour in magnitude, while a strong 486 one would be more than an hour (like the pictured example in Fig. 3A, bottom panel). 487 This computational approach extends our ability to detect phaseoids beyond those that 488 are visually detectable because their surrounds are active in the trough of the oscillation 489 to those that are active at any time of the oscillation. 490

491 Center-surround analyses of local phase comparisons reveal phaseoids

492 throughout the SCN. Identifying the phaseoids computationally allowed us to 493 determine whether local phase organization was reliant on the direction of the slice 494 and/or the part of the tissue that was sampled over any extent (Fig. 3B). This is 495 particularly relevant because intermediate structures have not been identified 496 previously. The results indicate that phaseoids exist regardless of the orientation of the 497 slices, but that their strength differs depending on the direction of slicing and the extent 498 of the SCN examined, particularly on the rostral-caudal axis. The local areas have 499 average phases that differ by roughly an hour regardless of slice orientation. This is 500 shown in Fig. 3B, by the color in the convolved map, which shows areas that are 501 advanced (blue) and delayed (yellow) relative to the surrounding tissue mean (green). 502 Note that phase differences in the local calculation are smaller than in the global 503 calculation due to averaging. Many pixels in the global phase map (on which the kernel 504 is convolved) are near the mean phase (i.e. phase difference of 0) and when included in 505 the local kernel this brings the average closer to zero. We truncated the color scale to 506 emphasize the pattern of local differences, even when the phaseoids are weak. The 507 brightest yellow and darkest blue regions can have local differences larger than one or 508 less than minus one respectively.

510 The strength of phaseoids differs across the SCN's rostral-caudal extent and

among slice orientations. In the sagittal and horizontal sections, phaseoids are stronger close to the rostral pole and weaker near the caudal extent (Fig. 3B, top two rows). We see this visually in the extent of the green areas (representing tissue mean) between the phase advanced (blue) and delayed (yellow) elements. In coronal sections, where the rostro-caudal extent is limited, we do not detect a consistent gradient on either the dorsal-ventral or medial-lateral axis (Fig. 3B, bottom row). As indicated in Fig 1A, the precise components of SCN tissue and the specific network components that are included in a slice will depend on precisely how it is blocked and cut. The coronal
 sections transect all rostro-caudal connections while this is not the case for sagittal and

520 horizontal slices.521

534 535

536

522 The magnitude of local phase differences is related to the global phase deviation.

523 Comparing the global phase estimates of the tissue (horizontal axis) to the local phase 524 differences (vertical axis) reveals an interesting relationship (Fig. 3C): Areas that lead 525 the mean oscillation by the largest amount tend to have large negative local phase 526 differences, while those that lag by the largest amounts tend to have large positive local phase differences. Including the ordinary least squares regression line (in red) reveals 527 528 positive linear slopes in each case. These results are statistically significant, with pvalues estimated below machine tolerance in every case (all $p < 10^{-16}$). If there were 529 530 no relations between local phase differences and the global properties of the oscillation, 531 we would expect no detectable correlation between global phase and local phase 532 differences and the regression line would be horizontal. Instead, we see a positive 533 correlation in each instance irrespective of orientation of the tissue.

Insert Fig. 3 about here

537 Legend Fig. 3: Local phase comparisons reveal phaseoids.

538 A. Center-surround filter is superimposed on a magnified view of a phase map. Upper panel: In the 539 center, there is a cell-sized region that is phase leading the mean signal. In the annular region, several 540 cell-sized areas are phase lagging the mean signal. This is consistent with evidence (Fig. 2) showing that 541 neighboring areas have different levels of expression in similar local spatial arrangements. Middle 542 panel: Cross-section of the center-surround filter used to compute the local phase differences. Lower 543 panel: Results of the local phase difference computation on the same region and with the same center 544 circle and surround annulus as the upper panel. The computation isolates the cell-sized regions and 545 identifies them as phase leading or phase lagging the neighboring pixels, allowing a full slice analysis of 546 local phase differences. The example shown here is the same phaseoid as that shown in Fig, 2A. Note 547 that the original observation of the phaseoid was by visual identification in the movie and it is well 548 captured by the filter (shown in Extended data Fig. 3-1).

549 B. Local phase differences as computed using the center-surround filter show numerous portions of the
550 SCN that are out of phase with their neighboring tissue. Sagittal and horizontal slices show a gradient
along the rostro-caudal axis where phase differences smaller at the caudal than the rostral aspect. The
colors in this figure have been truncated to emphasize differences in values close to zero. The green
border around the edge of each SCN is the result of "padding" to fill the kernel.

C. Plot of the global phase against the local phase difference to examine the relationship between the
 two. Each point represents a single pixel. On the horizontal axis (global phase estimate of the tissue),
 positive values indicate oscillation that lags the mean oscillation while negative values indicate leading
 the mean oscillation. Linear regression lines (red) have high statistical significance and support the
 hypothesis that areas with larger local differences are more strongly leading or lagging the mean.

560 Kuramoto models connect the magnitude of local phase differences with the

561 strength of local connectivity. We next asked what might be causing this rostral-562 caudal gradient. For non-chaotic systems of coupled oscillators, connection strength is 563 intimately related to the phase dynamics of the system, leading us to hypothesize that 564 the topology of the SCN connectome that is retained when slicing in different directions 565 gives rise to the observed gradients in phaseoid strength. To test this hypothesis, we 566 turn to mathematical modeling to examine the potential role of connectivity in the 567 creation and strength of the local phase differences. We created a mathematical 568 simulation encoding some of the properties of the SCN by constructing a 20 x 20 grid of 569 oscillators with identical intrinsic frequencies that are linked to each of their four nearest 570 neighbors. We change the connectivity by manipulating coupling strength, quadratically 571 decreasing it as we move across the grid from right to left horizontally (Fig. 4A). In this 572 depiction, the coupling strengths of two oscillators in the same vertical column are 573 identical, but oscillators in the same row have different strengths depending on their 574 locations in the grid.

576 We solved the associated Kuramoto system numerically over a period of 240 hours and 577 calculated the phase of each oscillator (500 trials). We then applied a center-surround 578 filter to the calculated phases, akin to the phaseoid detector described above (Fig. 3A). 579 For each vertical column of oscillators, we consider the distribution of phaseoid 580 strengths and compute their quartiles. Fig. 4B reports these quartiles as a function of 581 the horizontal coordinate of the oscillator within the grid. We compare size of the difference between the 75th percentile curve (yellow) and the 25th percentile curve (blue) 582 583 to assess the strength of the phaseoids as a function of coupling strength. The 584 difference between the lower and upper quartiles is more compact on the right-hand 585 than the left-hand side, indicating that the strength of the phaseoids decreases along 586 with the strength of coupling. These results provide evidence for the hypothesis that the 587 greater the phaseoid strength, the stronger the local coupling between the oscillatory 588 neurons (Fig. 4C).

590 Insert Fig. 4 about here

592 **Legend Fig. 4:** Kuramoto models connect the magnitude of local phase differences with the strength of local connectivity.

A. A schematic of the network connectivity we use in simulations using the Kuramoto coupled oscillator
 model. The differences in shading from right to left indicate quadratically growing strength of the nearest
 neighbor coupling in the model.

597 B. Results of applying the center-surround filter to simulated data over 500 trials. We report the quartiles of the distribution of local phase differences for each column of oscillators (as in A) as we move from right to left, showing that as the connectivity grows, so does the magnitude of the local phase differences.
600 C. A schematic summarizing the interpretation of the local phase differences in the context of simulation results. Comparing to simulation results provides evidence that connection strength is weaker at the caudal edge of sagittal and horizontal sections and grows as we move towards the rostral tip.

605 **Discussion**

SCN networks as accessible models of oscillation. It is increasingly clear that systems in the brain responsible for temporal representation at many timescales rely on specific network organizations to sustain their activity (Buzsâaki, 2006). Network oscillations can bias input selection, temporally link neurons into dynamic assemblies, and modulate synaptic plasticity. The SCN is a uniquely accessible empirical model to study oscillatory networks: it is self-contained, it controls behavior and is reflected in observable physiological responses throughout the body.

613

589

591

eNeuro Accepted Manuscript

614 What is new in this work: The present work further demonstrates that while individual 615 neurons oscillate, the rhythm in the SCN relies on the specific elements that are present 616 in the network as a whole: the tissue is the issue. The observed oscillation in real time 617 imaging of slices depends on what parts of the network are present after physical 618 transection, and on the spatial and temporal resolution at which the tissue is being 619 studied. Our use of biological, analytic and simulation tools demonstrate processes at 620 multiple levels of analysis from individual cells to local and global organization in SCN 621 networks and reveal the phaseoid as an intermediate, local unit of organization. While 622 previous research has not identified local phaseoid-like structures in the SCN, the present findings are consistent with other locally identified neural units in the brain, such 623 624 as the hypercolumns in area V1 (Hubel & Wiesel, 1968) and striosomes of the striatum 625 (Graybiel & Ragsdale, 1978) that constitute intermediate structures parallel to the 626 phaseoid. We have defined the strength of the phaseoid as the magnitude of phase 627 difference between the center and surrounding annulus of phase-locked cells. We find 628 that the strength of phaseoids varies in a systematic gradient across the tissue if the 629 rostral-caudal axis is preserved. Interestingly, this gradient of local organization of 630 phaseoids is aligned with a previously reported global phase gradient along the same 631 axis in tissue harvested from animals held in long daylengths (Yoshikawa et al., 2013). 632 The overall strength of the phaseoids is greater in the rostral aspect, which tends to 633 phase lag, and smaller in the caudal aspect which tends to phase lead in sagittal and horizontal slices (Fig. 2B, 3B). Furthermore, strong phaseoids with negative local 634 635 differences are associated with leading the global phase while strong phaseoids with 636 positive differences lag it (Fig. 3C) – which is to say the relationship between local 637 phase differences and global phase is positive regardless of how the tissue is cut. The 638 linkage between local and global organization highlights the potential functional role of 639 the phaseoids in integrating local oscillatory information – phaseoids are not merely 640 physical structures, but a mesoscale component of the machinery that allows the SCN 641 to construct and maintain a robust and consultable circadian rhythm. 642

643 Our consideration of phaseoids, by the nature of the data, is necessarily two-644 dimensional but in the full three-dimensional structure of the SCN, the phaseoids may 645 have more complex structures. The phaseoids we observe appear as rosettes. These 646 structures are supported by observations made by eye in the PER2::LUC imaging 647 movie frames, are also detected in fixed tissue, and are more fully revealed and 648 characterized in the analytic tool we developed. In an intact SCN, the three-649 dimensional structures of the phaseoids may take many possible topological types – 650 spheres, cylinders, tori (Harding et al., 2014). 651

We propose an impressively parsimonious model for the cause of these local/global
patterns seen in the rostro-caudal gradient of phaseoid strength. The Kuramoto
simulation results suggest that changes in strength of local coupling can produce similar
patterns in model systems. Stronger local connectivity leads to stronger phaseoids in
coupled oscillators (Fig. 4). It has been suggested that the brain clock network bears
properties of small world networks (Strogatz, 2001; Vasalou *et al.*, 2009; Hosseini &
Kesler, 2013), which have tight local coupling alongside some longer-range

connectivity. Our work helps to delineate possible structures for the local coupling,connecting it functionally to properties of the oscillation across the tissue.

Relationship to prior work. The results are consistent with previous descriptions of 662 phase in clusters of SCN neurons. The occurrence of individual neurons having 663 664 elevated PER2 protein at the overall trough of expression have previously been 665 reported: In prior work however, it was not known whether these cells oscillate in 666 antiphase with the larger population, or whether they are arrhythmic and continually express PER (Herzog et al., 1997; Hastings et al., 1999; Field et al., 2000; Nakamura et 667 al., 2001; LeSauter et al., 2003). Our results indicate that an antiphase population is 668 669 rhythmic, with high PER2 expression between ZT0 and ZT4 and low expression by ZT6 670 (Extended data Fig. 1-1).

671 While phase dispersal and phase waves have been described, the occurrence of 672 phaseoids or other intermediate structures has not been noted previously. Perhaps 673 these were seen but not investigated or, alternatively, this may be due to slice thickness. 674 Our slices in the real time imaging preparations are thin $(100\mu m)$, allowing for better 675 cellular resolution, while in many other laboratories, slice thickness is ~300µm. With 676 300µm slices, it is difficult to visualize many individual cells simultaneously. Thin slices 677 may have less of the global network than thick ones, but optimize single cell analysis. 678 Another factor maybe the use of noise reduction algorithms or use of megapixels, which 679 also reduce the resolution. Choices within these algorithms include decisions on how 680 many pixels to use to smooth the signal and how to smooth the signals, which could 681 have obscured phaseoids in prior reports. 682

683 Importance of phase heterogeneity for timekeeping. Physiological and behavioral 684 functions, including feeding, drinking, sleep-wake, body temperature, hormonal rhythms, 685 and enzyme activity, have circadian rhythms with specific circadian peaks. To 686 accurately assess circadian time at every time of day requires consulting cells whose 687 PER2 concentrations are changing over time. Phase heterogeneity in PER2 expression 688 allows this precise consultation throughout the circadian cycle, because at any phase of 689 the mean oscillation, some cells will have swiftly changing expression of PER2. While the present work focuses on expression of PER2, the principle of heterogeneity in 690 691 cellular rhythms applies more generally to cellular activity of a variety of responses. The 692 precise consultation throughout the circadian cycle is enabled because at any phase of 693 the mean oscillation, some cells will have rhythms at a particular phase. Our findings 694 imply, in addition to sequentially phased PER2 rhythms, phaseoids may enable even 695 more precise and specific regulations in overt rhythms.

696 An analogous finding in the visual system is that the neurons that provide the most 697 information about the orientation of an edge are those whose firing rates change the 698 most, rather than those that fire the most when presented with similarly oriented 699 direction of motion (Osborne et al., 2004). Protein concentrations of the mean signal in 700 the SCN overall change slowly, especially when they are near the peak or trough of 701 expression. Knowing the mean expression level of PER2 gives only a rough time signal 702 whether it is near the peak, trough or in between. Higher precision requires 703 information complementary to mean concentration: the rate of change in concentrations

704 of cells out of phase with the mean. Rapid changes in concentration within phasically 705 heterogeneous cells provide continuously accurate time of day information regardless of 706 the state of the mean oscillation. The advantages of this heterogeneity likely represent a 707 general property of information encoding in the brain.

709 **Extended Data**

708

710

713

714

717

718

719

720

723

724

725

726 727

728 729

730

731

732

733 734 735

736

737

738

739

740

741

742

743

744 745 746

747

748

749

750

711 Insert Extended Data Fig. 1-1, 2-1, 2-2, 3-1 712

Extended Data Fig. 1-1: PER2 expression at 2 hr. intervals in medial, mid- and lateral SCN. To localize changes in PER2 expression so as to have a baseline against which to compare the ex vivo 715 716 sagittal slices in the real time imaging experiments, we assessed expression of the protein through the entire SCN in fixed tissue at 2 hr. intervals. Female (N = 11) and male (N = 25) mice were perfused and brains were processed to stain for PER2 (as in (Riddle et al., 2017); rabbit anti-PER2 antibody used at 1:500: catalog # AB2202: RRID:AB 1587380. EMD Millipore Corporation, Temecula, CA), Sagittal sections of the SCN allowed visualization of the full rostro-caudal extent of the nucleus. Each dot represents the number and location of the PER2 nuclei observed in 2-3 brains at each time point. PER2-721 722 positive neurons can be seen at the trough of PER2 at ZT24/0 to ZT4 in the mid and lateral SCN in the mid-SCN. The rostral SCN expresses PER2 from ZT4 to ZT22. The photomicrographs in row 4 and 8 show the mid-SCN. The implication of regionally localized PER2 expression is that the observed network architectures will depend on the precise orientation of the slice. Maintaining the rostral and caudal poles of the SCN may preserve important circuit components that are lost in coronal sections.

Extended data Fig. 2-1: Post imaging immunohistochemical analysis of histology.

After imaging, sagittal slices (n = 22 slices, 100 um, from 6 mice) were fixed with 4% PFA after the bioluminescence recording, and immunohistochemically labeled with a cocktail of antibodies against AVP (AVP-NP, PS419) and VIP (Peptide Institute, 14110). Immunohistochemical staining was examined by fluorescent microscopy (BZ9000; Keyence, Osaka, Japan) as previously reported (Yoshikawa et al., 2015). A. Schematic drawing of the SCN. The blue lines indicate the plane of 100 micron sagittal slices that were made.. Numbers (-2 ~ +2) indicate position of the sagittal slices with respect to the midline.. B. Images of bioluminescence, immunohistochemical staining for AVP, VIP and overlay of AVP and VIP. C. Chart comparing robustness of oscillation and expression of AVP and VIP in each slice. Slice IDs indicate good (black) and poor (grey) rhythms. Number of immunopositive cell bodies for VIP and AVP are expressed in symbols. ++, high; +, medium; ±, low; -, none. Robust oscillation requires both AVP and VIP expression. Slices bearing a large number of AVP neurons but lacking VIP showed poor rhythm. The one slice that had both peptides could not classified with respect to rhythmicity due to technical equipment problems. Anatomical analysis of peptide expression was conducted independently and prior to classification of rhythmicity. The number of positive cell bodies were scored as follows: For VIP: >10 cells = ++, 5-9 cells = +, 1-4 cells = \pm , no cells = -. For AVP: >20 cells = ++, 5-20 cells = +, 1-5 cells = \pm , no cell = -.

Extended data Fig. 2-2. Phaseomes in fixed SCN tissue: Photomicrograph of a 50µm sagittal SCN section immunostained for PER2 (red) at ZT20. White asterisks show the location of phaseomes. The inset is a magnification of the phaseome indicated by the white arrow. Slices were processed for immunocytochemistry as in (Riddle et al., 2017).

751 Extended data Figure 3-1. This figure gives a comparison between manual identification of neurons that 752 are possibly out of phase with their surroundings and the results of the local phase difference 753 computations. The left panel shows a region of the SCN in a movie frame near the trough of the mean 754 oscillation of the tissue. In observing the movie, we could identify several neurons (marked with a red 755 asterisk) that seemed to be out of phase with much of the surrounding tissue. In the middle panel, 756 different intensities of green indicate the results of the local phase computations, with the more negative

phase differences shown in brighter green. The locations of the neurons from the first panel are marked with blue asterisks where the color scale indicates that they are oscillating between two and three hours behind the surrounding annular region. The right panel shows a merging of the two other panels, demonstrating that the higher intensity areas from the first panel coincides with more negative local phase differences from the second panel. The overlay creates magenta asterisks showing that the placement of the images coincides.

765 **References**

766 767

771

775

779

784

764

Abel, J.H., Meeker, K., Granados-Fuentes, D., John, P.C.S., Wang, T.J., Bales, B.B.,
 Doyle, F.J., Herzog, E.D. & Petzold, L.R. (2016) Functional network inference of
 the suprachiasmatic nucleus. *Proceedings of the National Academy of Sciences*,
 113, 4512-4517.

- Aton, S.J., Colwell, C.S., Harmar, A.J., Waschek, J. & Herzog, E.D. (2005) Vasoactive
 intestinal polypeptide mediates circadian rhythmicity and synchrony in
 mammalian clock neurons. *Nature Neuroscience*, **8**, 476-483.
- Brown, T.M. & Piggins, H.D. (2009) Spatiotemporal Heterogeneity in the Electrical
 Activity of Suprachiasmatic Nuclei Neurons and their Response to Photoperiod. J
 Biol Rhythm, 24, 44-54.
- 780 Buzsâaki, G. (2006) Rhythms of the brain. Oxford University Press,, Oxford ; New York.

781

- Buzsaki, G. & Draguhn, A. (2004) Neuronal oscillations in cortical networks. *Science*, **304**, 1926-1929.
- Canny, J. (1986) A computational approach to edge detection. *IEEE Transactions on pattern analysis and machine intelligence*, 679-698.
- Enoki, R., Kuroda, S., Ono, D., Hasan, M.T., Ueda, T., Honma, S. & Honma, K. (2012)
 Topological specificity and hierarchical network of the circadian calcium rhythm in
 the suprachiasmatic nucleus. *P Natl Acad Sci USA*, **109**, 21498-21503.
- Evans, J.A., Leise, T.L., Castanon-Cervantes, O. & Davidson, A.J. (2011) Intrinsic
 Regulation of Spatiotemporal Organization within the Suprachiasmatic Nucleus.
 Plos One, 6.

795

791

Favaretto, C., Cenedese, A. & Pasqualetti, F. (2017) Cluster Synchronization in
 Networks of Kuramoto Oscillators. *Ifac Papersonline*, **50**, 2433-2438.

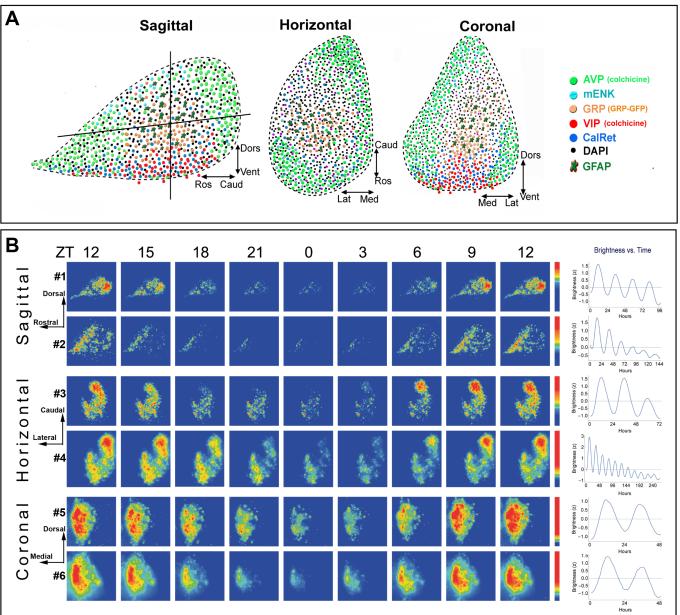
799 800 801 802	Field, M.D., Maywood, E.S., O'Brien, J.A., Weaver, D.R., Reppert, S.M. & Hastings, M.H. (2000) Analysis of clock proteins in mouse SCN demonstrates phylogenetic divergence of the circadian clockwork and resetting mechanisms. <i>Neuron</i> , 25, 437-447.
803 804 805	Finger, A.M. & Kramer, A. (2020) Mammalian circadian systems: organization and modern life challenges. <i>Acta Physiologica</i> , e13548.
806 807 808 809	Foley, N.C., Tong, T.Y., Foley, D., LeSauter, J., Welsh, D.K. & Silver, R. (2011) Characterization of orderly spatiotemporal patterns of clock gene activation in mammalian suprachiasmatic nucleus. <i>Eur J Neurosci</i> , 33 , 1851-1865.
810 811 812 813 814	Gloveli, T., Dugladze, T., Rotstein, H.G., Traub, R.D., Monyer, H., Heinemann, U., Whittington, M.A. & Kopell, N.J. (2005) Orthogonal arrangement of rhythm- generating microcircuits in the hippocampus. <i>P Natl Acad Sci USA</i> , 102 , 13295- 13300.
815 816 817 818	Graybiel, A.M. & Ragsdale, C.W. (1978) Histochemically distinct compartments in the striatum of human, monkeys, and cat demonstrated by acetylthiocholinesterase staining. <i>Proceedings of the National Academy of Sciences</i> , 75 , 5723-5726.
819 820 821 822	Harding, M.J., McGraw, H.F. & Nechiporuk, A. (2014) The roles and regulation of multicellular rosette structures during morphogenesis. <i>Development</i> , 141 , 2549-2558.
823 824 825 826 827	Hastings, M.H., Field, M.D., Maywood, E.S., Weaver, D.R. & Reppert, S.M. (1999) Differential Regulation of mPER1 and mTIM Proteins in the Mouse Suprachiasmatic Nuclei: New Insights into a Core Clock Mechanism. <i>The Journal</i> <i>of Neuroscience</i> , 19 , RC11-RC11.
828 829 830 831	Hastings, M.H., Maywood, E.S. & Brancaccio, M. (2018) Generation of circadian rhythms in the suprachiasmatic nucleus. <i>Nature Reviews Neuroscience</i> , 19 , 453-469.
832 833 834 835	Herzog, E.D., Geusz, M.E., Khalsa, S.B.S., Straume, M. & Block, G.D. (1997) Circadian rhythms in mouse suprachiasmatic nucleus explants on multimicroelectrode plates. <i>Brain research</i> , 757 , 285-290.
836 837 838 839	Honma, S. (2018) The mammalian circadian system: a hierarchical multi-oscillator structure for generating circadian rhythm. <i>J Physiol Sci</i> , 68 , 207-219.

840 841 842	Honma, S., Ono, D., Suzuki, Y., Inagaki, N., Yoshikawa, T., Nakamura, W. & Honma, Ki. (2012) Suprachiasmatic nucleus: cellular clocks and networks <i>Progress in brain research</i> . Elsevier, pp. 129-141.
843 844 845 846	Hosseini, S.H. & Kesler, S.R. (2013) Comparing connectivity pattern and small-world organization between structural correlation and resting-state networks in healthy adults. <i>Neuroimage</i> , 78 , 402-414.
847 848 849	Hubel, D.H. & Wiesel, T.N. (1968) Receptive Fields and Functional Architecture of Monkey Striate Cortex. <i>J Physiol-London</i> , 195 , 215-&.
850 851 852 853	Inagaki, N., Honma, S., Ono, D., Tanahashi, Y. & Honma, K. (2007) Separate oscillating cell groups in mouse suprachiasmatic nucleus couple photoperiodically to the onset and end of daily activity. <i>P Natl Acad Sci USA</i> , 104 , 7664-7669.
854 855 856 857	Indic, P., Schwartz, W.J., Herzog, E.D., Foley, N.C. & Antle, M.C. (2007) Modeling the behavior of coupled cellular circadian oscillators in the suprachiasmatic nucleus. <i>J Biol Rhythm</i> , 22 , 211-219.
858 859 860 861 862	Koinuma, S., Asakawa, T., Nagano, M., Furukawa, K., Sujino, M., Masumoto, K.H., Nakajima, Y., Hashimoto, S., Yagita, K. & Shigeyoshi, Y. (2013) Regional circadian period difference in the suprachiasmatic nucleus of the mammalian circadian center. <i>Eur J Neurosci</i> , 38 , 2832-2841.
863 864 865	LeSauter, J. & Silver, R. (1999) Localization of a suprachiasmatic nucleus subregion regulating locomotor rhythmicity. <i>J Neurosci</i> , 19 , 5574-5585.
866 867 868 869	LeSauter, J., Yan, L., Vishnubhotla, B., Quintero, J.E., Kuhlman, S.J., McMahon, D.G. & Silver, R. (2003) A short half-life GFP mouse model for analysis of suprachiasmatic nucleus organization. <i>Brain Res</i> , 964 , 279-287.
870 871 872 873 874	Nakamura, K., Kitani, A. & Strober, W. (2001) Cell contact–dependent immunosuppression by CD4+ CD25+ regulatory T cells is mediated by cell surface–bound transforming growth factor β. <i>The Journal of experimental</i> <i>medicine</i> , 194 , 629-644.
875 876 877 878 878	Osborne, L.C., Bialek, W. & Lisberger, S.G. (2004) Time course of information about motion direction in visual area MT of macaque monkeys. <i>J Neurosci</i> , 24 , 3210-3222.
0.7	

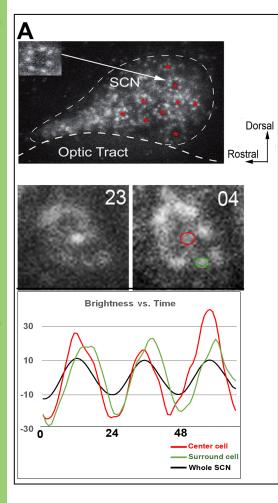
880 881 882 883 884	Pauls, S., Foley, N.C., Foley, D.K., LeSauter, J., Hastings, M.H., Maywood, E.S. & Silver, R. (2014) Differential contributions of intra-cellular and inter-cellular mechanisms to the spatial and temporal architecture of the suprachiasmatic nucleus circadian circuitry in wild-type, cryptochrome-null and vasoactive intestinal peptide receptor 2-null mutant mice. <i>Eur J Neurosci</i> , 40 , 2528-2540.
885 886 887	Pauls, S.D., Honma, K.I., Honma, S. & Silver, R. (2016) Deconstructing Circadian Rhythmicity with Models and Manipulations. <i>Trends Neurosci</i> , 39 , 405-419.
888 889 890	Quintero, J.E., Kuhlman, S.J. & McMahon, D.G. (2003) The biological clock nucleus: A multiphasic oscillator network regulated by light. <i>J Neurosci</i> , 23 , 8070-8076.
891 892 893 894	Riddle, M., Mezias, E., Foley, D., LeSauter, J. & Silver, R. (2017) Differential localization of PER 1 and PER 2 in the brain master circadian clock. <i>Eur J Neurosci</i> , 45 , 1357-1367.
895 896 897 898	Rusak, B. (1977) The role of the suprachiasmatic nuclei in the generation of circadian rhythms in the golden hamster, Mesocricetus auratus. <i>Journal of comparative physiology</i> , 118 , 145-164.
899 900 901	Schaap, J., Pennartz, C.M. & Meijer, J.H. (2003) Electrophysiology of the circadian pacemaker in mammals. <i>Chronobiology international</i> , 20 , 171-188.
902 903	Strogatz, S.H. (2001) Exploring complex networks. Nature, 410, 268-276.
904 905 906 907	Tokuda, I.T., Ono, D., Honma, S., Honma, KI. & Herzel, H. (2018) Coherency of circadian rhythms in the SCN is governed by the interplay of two coupling factors. <i>PLoS computational biology</i> , 14 , e1006607.
908 909 910	Van den Pol, A.N. (1980) The Hypothalamic Suprachiasmatic Nucleus of Rat - Intrinsic Anatomy. <i>J Comp Neurol</i> , 191 , 661-702.
911 912 913 914	Varadarajan, S., Tajiri, M., Jain, R., Holt, R., Ahmed, Q., LeSauter, J. & Silver, R. (2018) Connectome of the Suprachiasmatic Nucleus: New Evidence of the Core-Shell Relationship. <i>Eneuro</i> , 5 .
915 916 917 918	Vasalou, C., Herzog, E.D. & Henson, M.A. (2009) Small-World Network Models of Intercellular Coupling Predict Enhanced Synchronization in the Suprachiasmatic Nucleus. <i>J Biol Rhythm</i> , 24 , 243-254.
919	

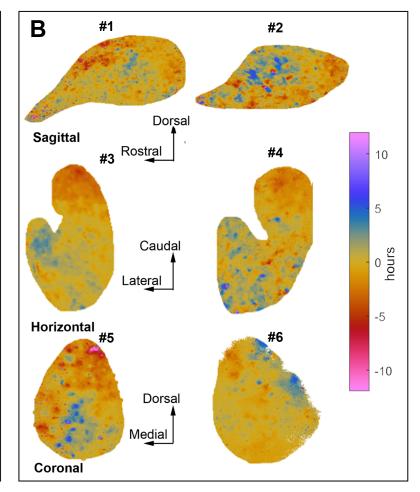
920 921 922 923	Wang, S., Herzog, E.D., Kiss, I.Z., Schwartz, W.J., Bloch, G., Sebek, M., Granados- Fuentes, D., Wang, L. & Li, JS. (2018) Inferring dynamic topology for decoding spatiotemporal structures in complex heterogeneous networks. <i>Proceedings of</i> <i>the National Academy of Sciences</i> , 115 , 9300-9305.
924 925 926 927	Webb, A.B., Angelo, N., Huettner, J.E. & Herzog, E.D. (2009) Intrinsic, nondeterministic circadian rhythm generation in identified mammalian neurons. <i>P Natl Acad Sci</i> USA, 106 , 16493-16498.
928 929 930 931 932	Wen, S.A., Ma, D.Y., Zhao, M., Xie, L.C., Wu, Q.Q., Gou, L.F., Zhu, C.Z., Fan, Y.Q., Wang, H.F. & Yan, J. (2020) Spatiotemporal single-cell analysis of gene expression in the mouse suprachiasmatic nucleus. <i>Nature Neuroscience</i> , 23 , 456-+.
933 934 935 936	Yamaguchi, S., Isejima, H., Matsuo, T., Okura, R., Yagita, K., Kobayashi, M. & Okamura, H. (2003) Synchronization of cellular clocks in the suprachiasmatic nucleus. <i>Science</i> , 302 , 1408-1412.
937 938 939	Yan, L.L. & Okamura, H. (2002) Gradients in the circadian expression of Per1 and Per2 genes in the rat suprachiasmatic nucleus. <i>Eur J Neurosci</i> , 15 , 1153-1162.
940 941 942 943	Yoshikawa, T., Inagaki, N.F., Takagi, S., Kuroda, S., Yamasaki, M., Watanabe, M., Honma, S. & Honma, K. (2017) Localization of photoperiod responsive circadian oscillators in the mouse suprachiasmatic nucleus. <i>Sci Rep-Uk</i> , 7 .
944 945 946 947	Yoshikawa, T., Matsuno, A., Yamanaka, Y., Nishide, S., Honma, S. & Honma, K. (2013) Daily exposure to cold phase-shifts the circadian clock of neonatal rats in vivo. <i>Eur J Neurosci</i> , 37 , 491-497.
948 949 950 951 952	 Yoshikawa, T., Nakajima, Y., Yamada, Y., Enoki, R., Watanabe, K., Yamazaki, M., Sakimura, K., Honma, S. & Honma, K. (2015) Spatiotemporal profiles of arginine vasopressin transcription in cultured suprachiasmatic nucleus. <i>Eur J Neurosci</i>, 42, 2678-2689.
953 954	
234	





aio Accepted Mallusci I





eNeuro Accepted Manuscript

